PHYSICAL REVIEW B **108**, 075139 (2023)

Electron confinement in chain-doped transition metal dichalcogenides: A platform for spin-orbit coupled one-dimensional physics

Mayank Gupta,[1,2,*] Amit Chauhan,[1,2,*] S. Satpathy,[1,2,3,†] and B. R. K. Nanda[1,2,‡]
[1]*Condensed Matter Theory and Computational Lab, Department of Physics, IIT Madras, Chennai 600036, India*
[2]*Center for Atomistic Modelling and Materials Design, IIT Madras, Chennai 600036, India*
[3]*Department of Physics & Astronomy, University of Missouri, Columbia, Missouri 65211, USA*

(Received 26 March 2023; revised 11 July 2023; accepted 28 July 2023; published 17 August 2023)

State-of-the-art defect engineering techniques have paved the way to realize unique quantum phases out of pristine materials. Here, through density-functional calculations and model studies, we show that the chain-doped monolayer transition metal dichalcogenides, where M atoms on a single zigzag chain are replaced by a higher-valence transition-metal element M' (MX_2/M'), exhibit one-dimensional (1D) bands. These 1D bands, occurring in the fundamental gap of the pristine material, are dispersive along the doped chain but are strongly confined along the lateral direction. This confinement occurs as the bare potential of the dopant chain formed by the positively charged M' ions resembles the potential well of a uniformly charged wire. These bands could show unique 1D physics, including another type of Tomonaga-Luttinger liquid behavior, multiorbital Mott insulator physics, and an unusual optical absorption due to the simultaneous presence of the spin-orbit coupling, strong correlation, multiple orbitals, Rashba spin splitting, and broken symmetry. We find the broadening of the half-filled 1D bands with correlation. It is surprising since correlation reduces the effective hopping interactions and in turn reduces the bandwidth. This is interpreted to be due to multiple orbitals forming the single Hubbard band at different points of the Brillouin zone. Furthermore, due to the presence of an intrinsic electric field along the lateral direction, the 1D bands are Rashba spin-split and provide a mechanism for tuning the valley-dependent optical transitions.

DOI: 10.1103/PhysRevB.108.075139

I. INTRODUCTION

Successful synthesis of atomistically controlled van der Waals layered materials in the form of transition metal chalcogenides (TMDs) has given rise to a wide range of mesoscopic nontrivial quantum phases. These include proximity of p-wave superconductivity and charge density wave as in $NbSe_2$ [1–3], topological Weyl semimetallic nature and large magnetoresistance as in WTe_2 [4–6], and the exotic orbital and quantum spin Hall effects [7–9].

One of the emerging areas of research on two-dimensional (2D) TMDs is to further reduce the dimensionality and explore subnanoscale quantum physics. For example, the Moirè bilayers of TMDs and their heterostructures allow twist angle controlled resonant effects to engineer exciton band structures [10,11]. The lateral superlattices and nanoribbons are synthesized out of TMDs to produce edge and interfacial states [12–17]. A recent study has proposed a typical moirè lattice out of WTe_2, where an overarching periodicity creates a one-dimensional (1D) lattice for electrons residing in collective eigenstates which give rise to rarely observed exotic quantum states of Tomonaga Luttinger liquid (TLL) behavior [12]. The ribbon edge states in 1-T′-WTe_2 exhibiting TLL behavior is an experimental result in this direction [15]. The TLL state is also experimentally observed in MoS_2 by creating mirror twin boundaries [16]. Electron correlation is an important missing factor in TMDs and, therefore, correlation-driven exotic quantum phases in the area of magnetism and superconductivity are less evident in this class of compounds. To achieve the correlated electron phases, narrow bands in the vicinity of Fermi energy need to be created, and one of the ways to make it possible is to confine the electron motion by reducing the dimensionality.

Unlike the semimetallic 1T′ phase [18], the 2H phase of TMDs has wide band gaps and hence unique quantum phases and transport can be envisaged in them by inducing midgap states of lower dimensions. With growing interest in doped 2D TMDs, there are experimental proposals on tunable doping mechanisms in these systems [19]. Recently, Lin *et al.* [20] reported excellent controllability for substitutional doping of the foreign atoms in 2D TMDs through low-energy ion implantation techniques such as site-selective laser-assisted chemical vapor doping [21]. Furthermore, a very recent experimental work demonstrated a controlled doping strategy for TMDs based on a dislocation climb mechanism [22]. In this reference, the authors were successful in forming highly doped nanostripes of Ti, V, Cr, and Fe atoms in WSe_2 and WS_2 monolayers.

In this paper, we have engineered 1D quantum states out of the semiconducting 2H phase of MoX_2 and WX_2 monolayers, with X being a chalcogen. This is achieved by replacing a

---

[*] These authors contributed equally to this work.
[†] SatpathyS@missouri.edu
[‡] nandab@iitm.ac.in

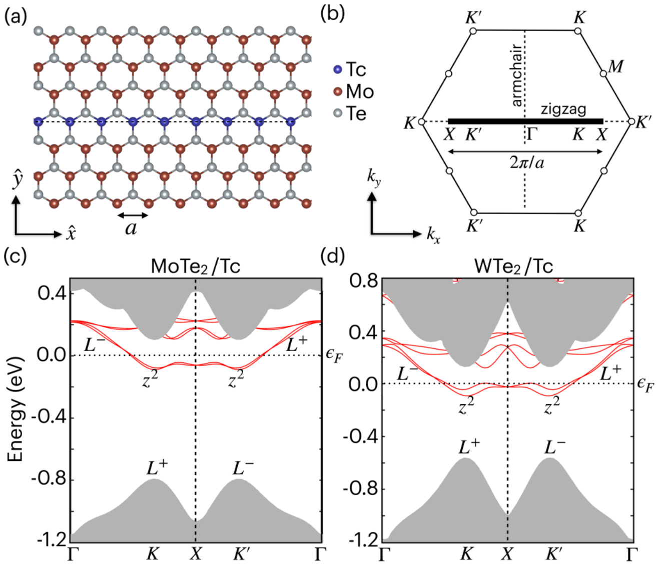

FIG. 1. (a) Top view of the chain-doped MX_2/M' compound, where a single zigzag chain of the pristine MX_2 structure is replaced with an $M'X_2$ chain. (b) The reduced 1D Brillouin zone (line extending between $-\pi/a < k_x < \pi/a$) for the chain-doped structure and its relation to the original 2D Brillouin zone (hexagon). All three valley points K of the hexagonal BZ fall onto the same point, marked by K, on the 1D BZ, and the same happens for the K' points. The hexagonal zone collapses vertically onto the k_x axis, and the points lying outside the 1D BZ in the process are brought inside it via the reciprocal lattice translation of $2\pi/a$. The zigzag/armchair labels in the figure indicate the orientation of the BZ with respect to the crystalline directions in real space. (c), (d) The DFT+SOC band structure of the pristine $MoTe_2$ and WTe_2 (shaded grey), projected into the 1D BZ. The red lines indicate the defect bands introduced by the Tc doped chain in the forbidden region. These bands represent 1D propagating states along the chain, while they are confined in the lateral direction. The defect bands are dominated by the orbital characters of Tc. The small splitting of the otherwise degenerate defect bands is because of the Rashba SOC due to a nonzero lateral electric field (see text).

single chain of Mo or W along the zigzag direction with an element M' with one extra valence electron as shown in Fig. 1. We find these chain-doped systems, henceforth represented as MX_2/M' to be dynamically stable. The 1D bands, depending on several other factors, build a perfect platform to induce nontrivial low-dimensional quantum phases, which may include Peierls distortion [23], topological magnons [24], charge density waves [25], TLL [26], and 1D magnetism.

In the case of MTe_2/Tc and MTe_2/Re, we find that the weakly SOC-driven degenerate half-filled 1D bands running along the chain make them ideal candidates for exhibiting TLL phenomena. In the magnetic phase, the effect of strong correlation can produce Mott insulating states by breaking the half-filled 1D bands to lower and upper Hubbard subbands with a gap in between. However, a phenomenon emerges where the on-site Coulomb repulsion, instead of localizing, delocalizes the lower Hubbard subbands. Upon practical realization, it can give rise to an unusual 1D quantum transport. The dopant chain breaks the reflection symmetry to introduce an intrinsic electric field along the lateral direction. This, in turn, makes the 1D bands Rashba spin-split and introduces valley-dependent optical transition in the system.

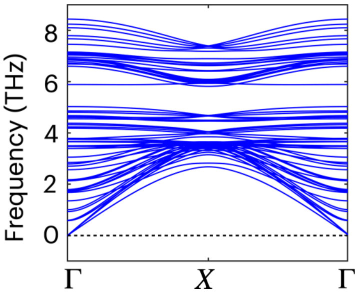

FIG. 2. The phonon frequencies of the chain-doped $MoTe_2/T_c$ ($Mo_6Tc_1Te_{14}$). The force constants obtained from the DFPT method are taken into account through the PHONOPY code [27] as implemented in VASP. The absence of imaginary modes implies the dynamical stability of the chain-doped structure.

II. STRUCTURAL AND COMPUTATIONAL DETAILS

The prototype representation of the chain-doped monolayer structures ($MX_2/\mathrm{M}' = \mathrm{M}_{n-1}\mathrm{M}'_1\mathrm{X}_{2n}$) is shown in Fig. 1(a). A detailed description of $M'X_2$ chain formation in a monolayer sheet of TMD is given in Sec. I of the Supplemental Material (SM) [29]. We have adopted the supercell approach with $n = 13$, which is found to be sufficient to induce the 1D defect bands. The phonon band structures of such systems do not show imaginary frequencies (see Fig. 2), suggesting dynamical stability. We have further calculated the formation energy of all chain-doped MX_2/M' compounds which suggest the thermodynamical stability of systems. The results are provided in the Sec. II of the SM. With chain doping along the zigzag direction, the 2D Brillouin zone (BZ) reduces to a 1D BZ as shown by a thick black strip in Fig. 1(b). The high-symmetry points of the 2D BZ are projected onto the reduced BZ, which helps us later in discussing the resonance and bound states. The density functional theory (DFT) calculations are carried out on optimized $M_{n-1}M'_1X_{2n}$ structures using the pseudopotential based projector-augmented wave method [30,31] within the framework of PBE-GGA exchange-correlation functional as implemented in the VIENNA AB INITIO SIMULATION PACKAGE (VASP) [32]. The plane-wave energy cutoff of 400 eV is used. For structural relaxation, while a $1\times8\times1$ Γ-centered k-mesh is used for BZ integration, self-consistency of the charge density is obtained with a $1\times8\times2$ k-mesh. The thickness of vacuum layer in the z direction is taken to be 15 Å. The Hubbard U formalism is adopted to study the correlation effect arising due to localized defect states. The U values are obtained using the linear response theory [33]. The cell-averaged bare potential is calculated using the QUANTUM ESPRESSO simulation package [34].

III. FORMATION OF 1D BANDS

While a range of chain-doped configurations are investigated, here we will discuss the electronic structure of $MoTe_2/T_c$ and WTe_2/T_c as prototypes. However, it is useful to first provide a brief overview of the electronic structure

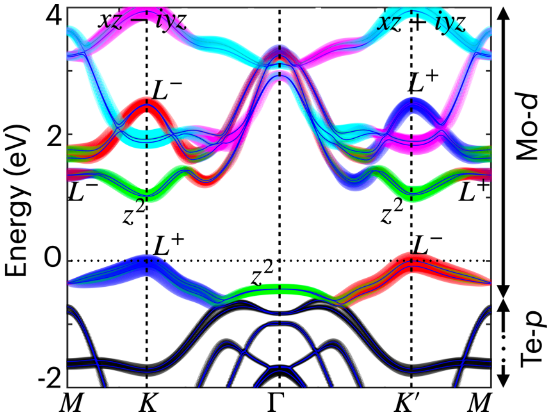

FIG. 3. The orbital-resolved band structure of the monolayer $MoTe_2$ obtained using WANNIER90 [28]. The valence band maximum occurring at the valley points, K and K', are dominated by the angular momentum orbitals $L^{\pm} = (x^2 - y^2 \pm ixy)$, while the conduction band minima are formed by the z^2 orbital, all belonging to the Mo atom. The spectrum below the top valence band is formed by the Te-p states.

of the pristine TMDs so the formation of the dopant states can be better understood. For this purpose, in Fig. 3, we present the band structure of monolayer 2H-$MoTe_2$ [35]. The electronic properties of the TMDs have been widely studied [35–37]. The formation of bands can be described with two-step chemical bonding. In the first step, the nearest-neighbor Mo-d–Te-p interactions give rise to lower-lying Te-p dominated bands and upper-lying Mo-d dominated bands. Driven by the trigonal prismatic crystal field, the latter is further split into three groups: $A_1'(z^2)$, $E'(xy,\ x^2 - y^2)$, and $E''(xz,\ yz)$. The second step involves second-neighbor interactions where in the monolayer limit the reflection symmetry along the $\hat{z}$ direction permits hybridization among the A_1' and E' orbitals to create a band gap. The valley points K and K' host both the valence band maximum (VBM) and the conduction band minimum (CBM). The VBM at K and K' are found to be formed by $x^2 - y^2 + ixy$ (L^+) and $x^2 - y^2 - ixy$ (L^-) orbitals, respectively, giving rise to opposite orbital moments [8] while the CBM is formed by the z^2 character and hence with zero orbital moments [8,35]. The role of the spin-orbit coupling (SOC) in this compound is restricted to splitting the bands dominated by L^+ and L^- by a few meV without perturbing the broad band structure. To produce unique quantum transport phenomena, the midgap states with varying characters can be generated in these systems through hole or electron doping.

The band structures of the chain-doped systems $MoTe_2/Tc$ and WTe_2/Tc are, respectively, shown in Figs. 1(c) and 1(d). The gray shaded region represents the bands of pristine $MoTe_2/(WTe_2)$ projected along $k_y = 0$ [see Figs. 1(c) and 1(d)]. The red bands belong to the chain-doped compounds. Most of them overlap with the bands of the parent compound, but the rest form defect bands, creating either bound states by lying in the forbidden region or resonating states by overlapping with the bulk bands. The defect bands lying in the vicinity of the Fermi level (ϵ_F) are of significant importance as they can introduce different transport behavior in the system. Our orbital projection analysis indeed shows that these bands are formed by the xy, $x^2 - y^2$, and z^2 orbitals of the Tc chain. Furthermore, the defect bands are dispersive along the chain direction while remaining bound perpendicular to it, and thereby a platform for 1D quantum physics is created.

The basic electronic configuration enables us to explain the formation of the 1D quantum state. In the semiconducting $MoTe_2$ and WTe_2, Mo^{4+} and W^{4+} have d^2 configuration. When Tc is doped, the Tc^{4+} has d^3 electronic configuration out of which two electrons (assume it as d^2) participate in maintaining the bulk semiconducting band structure while the remaining d electron (assume it as d^1) occupies the defect state which becomes half filled. In the case of chain doping, this leads to the formation of 1D band.

By giving away the additional electron (d^1), the Tc chain becomes positively charged. To estimate the resulting potential well, we have approximated the 1D chain to be a cylindrical wire of radius R_0. From Gauss's law, the potential inside and outside the wire can be expressed as

$$V = \begin{cases} \frac{\rho}{4\epsilon_r\epsilon_0} r^2, & r < R_0 \\ \frac{\rho R_0^2}{4\epsilon_0\epsilon_r}\left(1 + 2\log\left(\frac{r}{R_0}\right)\right), & r > R_0, \end{cases} \tag{1}$$

where $\rho = e/\pi R_0^2 a$ is the charge density of the wire, with a being the lattice constant. Based on the earlier theoretical studies, the dielectric constant (ϵ_r) is taken to be 20 [38]. We mapped the modeled potential with the cell-averaged bare potential obtained from the DFT calculations on a $MoTe_2/Tc$ superlattice. There is excellent agreement capturing both r^2 and logarithmic behavior inside and outside the wire, respectively, for $R_0 = 2.6$ Å, which is higher than the atomic radii of Tc and lower than the lattice parameter.

The wave functions of the ground and first two excited states [$\psi_n(r)$] and their corresponding eigenvalues (ε_n) are shown in Fig. 4(a), lower panel, which were obtained from the numerical solution to the one-particle Schrödinger equation with the potential given in Eq. (1). The eigenstates resemble those of the Airy functions which are the solutions of the Schrödinger equation at linearly varying potential wells [39]. The $|\psi_1(r)|^2$ plotted in a blue solid line in the upper half of Fig. 4(a) reflects the charge spread away from the Tc chain. For validation, we computed the cell averages of $|\psi_1(r)|^2$ (black filled squares) along the direction perpendicular to the chain and compared them with the atomwise contribution of the partially occupied lower lying defect band—values are depicted through the red filled circles—and found a very good match among them. The rapid exponential decay of the charge spread is also demonstrated through the logarithmic charge density [$\rho_{\mathrm{DFT}}(r)$] contours calculated for the 1D band. The $\rho_{\mathrm{DFT}}(r)$ is calculated by integrating the lower lying defect band up to ϵ_F. From Fig. 4(b), we observe that the spread vanishes after three layers on either side of the Tc chain while accumulating most of the charge on the chain itself. This implies that the defect state is bound laterally and dispersive along the Tc chain.

IV. PLATFORM FOR 1D PHYSICS

A. Rashba SOC and valley-dependent optical transitions

The partially filled nondegenerate defect bands can be fitted with a tight-binding model on the doped chain along with

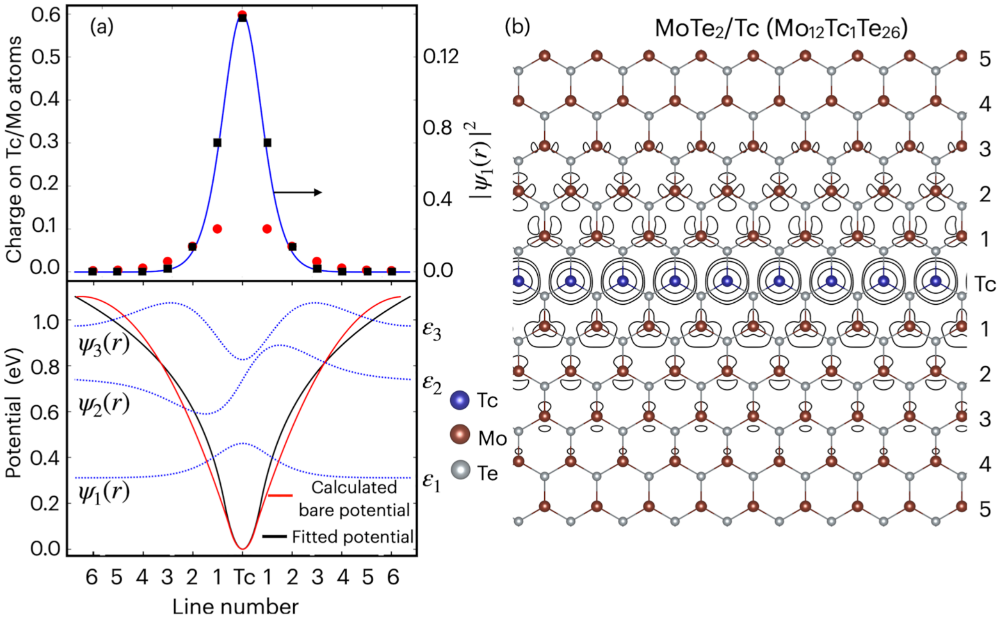

FIG. 4. The confinement of the chain-doped bands along the lateral direction. (a) Lower panel: The cell-averaged bare potential (red solid line) and the model potential (black solid line) as per Eq. (1). The ground- and the first two excited-state wave functions (ψ_1, ψ_2, and ψ_3) are sketched by blue dotted lines. These are obtained by numerically solving the Schrödinger equation for the model potential. Upper panel: The spread of the extra valence electron in this potential. The DFT obtained values are shown by red circles. The cell average of the ground-state charge density ($|\psi_1(r)|^2$) is shown by black squares. (b) Charge-density contours (isosurface value = 0.0001 $e/\text{Å}^3$) of the partially occupied defect bands as obtained by integrating from the bottom of the defect bands to the Fermi energy (see the red bands in Fig. 1).

a Rashba-like term, viz.,

$$\varepsilon(k) = (\varepsilon_0 + 2t\cos k_x + 2t'\cos 2k_x + 2t''\cos 3k_x)I + \lambda_R(\hat{E} \times \vec{k}) \cdot \vec{\sigma}, \tag{2}$$

where the chain runs along $\hat{x}$; ε_0 is the on-site energy taken to be zero; t, t', and t'' are, respectively, the hopping to the first-, second-, and third-nearest neighbors. Here, I is the 2×2 identity matrix and $\vec{\sigma}$ are Pauli spin matrices. λ_R is the Rashba strength. From the symmetry of the structure [Fig. 4(b)], an electric field exists in the y direction on the plane, which translates to a magnetic field $\vec{B} = \vec{v} \times \vec{E}/c^2$ in the electron's rest frame that couples to the spin moment. This leads to the spin-split band structure with a linear dispersion described by the last term in Eq. (2).

The TB parameters, obtained by fitting to the DFT results, are listed in Table I for a number of chain-doped compounds. We note that there is a substantial second-neighbor hopping t', but the third-neighbor hopping is substantial only for the Re chains and negligible for the Tc chains. The TB bands fitted with DFT for WTe_2/Tc are shown in Fig. S2 of the SM. Similar models can also be developed for the Rashba spin-split defect bands that lie in the forbidden regions other than the fundamental gap. The schematic band structure along with the Rashba spin splitting is illustrated in Fig. 5, which suggests interesting valley-dependent optical properties. In the parent MX_2 material, circularly polarized light with opposite polarization is absorbed at the two different valleys K and K'. Due to the Rashba-like spin splitting, we predict the chain-doped compounds to exhibit additional features in the valley-dependent optical absorption between the bulk to the defect states. The lowest-energy optical transitions at the valley points are forbidden because the lower defect band has spin opposite to that of the bulk valence band edge. Note that the projected bands onto the 1D BZ of the chain-doped compound not only shows the fundamental gap extending through the full BZ, but also gaps that exist at certain regions of the BZ as indicated for the valence bands in Fig. 5. As also indicated in the figure, localized 1D bands can exist within these gaps, and valley-dependent optical transitions would occur between these states, including the localized 1D bands lying in the fundamental gap. To illustrate, the dipole allowed lowest-energy optical transitions (σ^+ and σ^-) between partially filled and localized 1D conduction bands in the vicinity of valley points are indicated in the figure.

TABLE I. Rashba strength (in eV/Å) and the hopping integrals (in eV) for the 1D defect bands in MX_2/M', which are obtained by fitting Eq. (2) with the 1D half-filled defect bands.

Compound name	λ_R	t	t'	t''
MoSe_2/Tc	0.10	−0.053	0.032	0.003
MoSe_2/Re	0.76	−0.049	0.035	0.019
MoTe_2/Tc	0.10	−0.070	0.026	0.007
MoTe_2/Re	1.00	−0.077	0.030	0.019
WS_2/Tc	0.00	−0.041	0.039	0.002
WSe_2/Tc	0.20	−0.057	0.044	0.000
WTe_2/Tc	0.74	−0.090	0.048	0.007
WTe_2/Re	0.68	−0.081	0.041	0.025

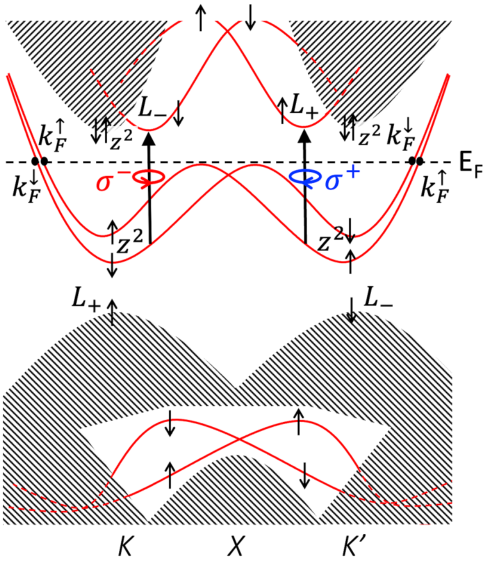

FIG. 5. Schematic 1D defect bands indicating the Rashba spin splitting and valley-dependent optical absorption. The shaded bands indicate the band structure of the 2D host material, while the red lines indicate the localized 1D defect bands introduced in the band gap of the host. The red dashed lines in the valence band indicate resonance states. Some dipole-allowed optical transitions for circularly polarized light are indicated by σ^- and σ^+. The orbital-projected bands of prototype WTe$_2$/Tc are shown in Fig. S3 of the SM.

B. Electronic correlation

Electron correlation effects are expected to be important for the 1D defect bands, since the bandwidth is quite narrow. A key parameter for characterizing the strength of the correlation effects is the on-site Coulomb repulsion U, which we now proceed to compute using DFT and the linear response approach.

In this method [33], U is computed by calculating the difference between interacting and noninteracting density response functions,

$$U = \chi_0^{-1} - \chi^{-1} = \left(\frac{\partial n_i^{\mathrm{KS}}}{\partial \alpha_i}\right)^{-1} - \left(\frac{\partial n_i}{\partial \alpha_i}\right)^{-1}, \tag{3}$$

where α_i is a perturbative shift in the single-particle potential at site i, for which U is being computed. Since the bandwidth of the d bands of the host compound MX_2 are rather large, and the bands are either occupied or unoccupied, the correlation effects are relatively weak. In contrast, the defect bands are 1D, relatively narrow, and half filled, so the correlation effects are expected to be important there. Therefore, we compute U only for the 1D defect bands. To obtain the response functions, the variation in occupation numbers is obtained by performing the DFT calculations in two ways: (i) by allowing the Kohn-Sham potential to adjust self-consistently, which optimally screens the perturbation α_i to give χ_0, and (ii) by calculating the Kohn-Sham potential without screening to get χ. The latter is achieved by a single loop, without enforcing self-consistency. The variation of n_i^{KS} and n_i as a function of α_i at the doped metal site (Tc or Re) is shown in Fig. 6 for MoSe$_2$/Tc and MoSe$_2$/Re. The on-site Coulomb repulsion U_0 calculated with this procedure is listed for various chain-doped compounds in Table II, together with the Fermi velocity v_F and the bandwidth W. The spin-resolved Fermi velocities $v_F^\uparrow$ and $v_F^\downarrow$ are computed at the Fermi momentum $k_F^\uparrow$ and $k_F^\downarrow$, which is roughly halfway along the $\Gamma - X$ line (see Figs. 1 and 7), by taking the derivative of the energy $\hbar v_F^{\uparrow\downarrow} = (\partial E^{\uparrow\downarrow}(k)/\partial k)_{k=k_F^{\uparrow\downarrow}}$. $k_F^\uparrow$ and $k_F^\downarrow$ differ as the SOC makes the spin-resolved bands nondegenerate. As seen from Table II, $U/W \gg 1$ for all compounds studied, which would put these materials in the strong correlation limit.

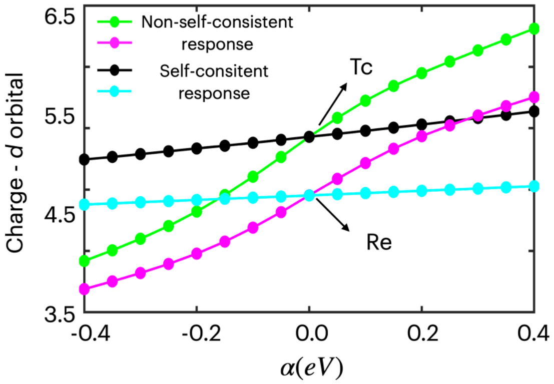

FIG. 6. Calculation of the Coulomb repulsion U_0 for the metal atom on the doped chain, Tc or Re, using Eq. (3). Plotted are the occupation numbers, n_i^{KS} and n_i, as a function of the perturbing potential α at the doped metal site, obtained using 1×4 supercell of MoSe$_2$/Tc and MoSe$_2$/Re, i.e., (M$_{n-1}$M$'_1$X$_{2n}$, $n = 7$)×4, where the perturbing potential was applied to a single Tc or Re atom.

C. Tomonaga Luttinger-Liquid physics

The low-energy behavior of the correlated electrons in 1D is described by the TLL theory, with features generic to many interacting 1D electron systems, such as the spin-charge separation and the anomalous scaling of the correlation functions [40–46]. A few years ago, the TLL theory was extended to include SOC. When SOC is introduced, the complete spin-charge separation is destroyed, resulting in mixed bosonic excitations involving these two degrees of freedom. However, the anomalous scaling of the correlation functions remains with modified exponents [47,48]. The TLL with SOC has been studied experimentally in the context of quasi-1D systems

TABLE II. Characteristics of the 1D defect band for various compounds. U, W, and v_F are the on-site Coulomb repulsion, bandwidth, and Fermi velocity, respectively.

Compound/ doping element	U(eV)	W(eV)	$v_{F\uparrow}$(eVÅ)	$v_{F\downarrow}$(eVÅ)
MoTe$_2$/Tc	1.65	0.30	0.67	0.78
MoSe$_2$/Tc	1.63	0.26	0.41	0.50
WTe$_2$/Tc	1.65	0.34	0.50	0.73
WSe$_2$/Tc	1.63	0.31	0.64	0.76
WS$_2$/Tc	1.30	0.20	0.43	0.76
MoSe$_2$/Re	4.99	0.24	0.82	0.58
MoTe$_2$/Re	4.90	0.27	1.01	0.69
WTe$_2$/Re	4.96	0.31	1.11	0.73

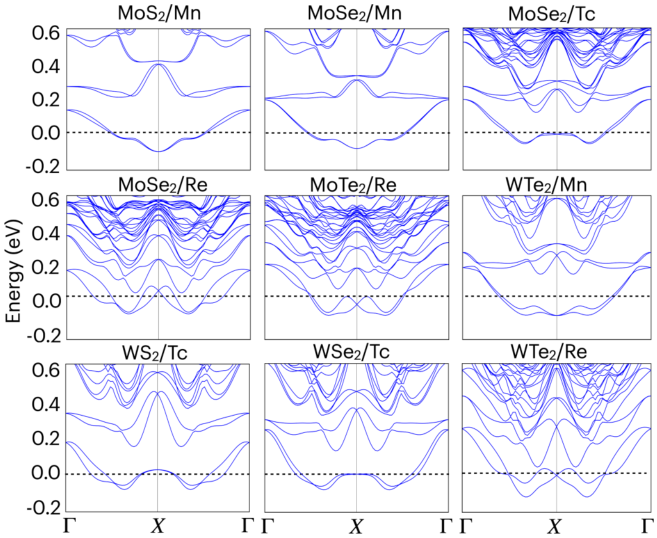

FIG. 7. The nonmagnetic band structures of several chain-doped compounds. The SOC is included.

such as the carbon nanotubes, quantum wires, and 2D electron gases confined to a narrow channel by gate electrodes, but much remains to be done both from theoretical and experimental points of view.

We propose the chain-doped TMDs to be an important class of materials to study TLL physics, including the effect of SOC. As illustrated for a number of cases in Figs. 1 and 7, the defect bands in the chain-doped TMDs are spin split at the Fermi energy to a varying degree due to the SOC. For example, the splitting is near zero for MoTe_2/Tc, while it is quite large for WS_2/Tc. The 1D defect bands in the chain-doped TMDs are nominally half filled, for which the TLL behavior would be absent [49]. However, departure from the half-filling scenario can occur naturally due to the presence of impurities and/or applied gate voltage, which may furthermore be used to alter the spin-splitting at the Fermi energy. Thus, the chain-doped TMDs may serve as a rich laboratory for the study of TLL behavior. Another interesting area of study of the metallic 1D system is the magnetic behavior in the presence of the SOC [50], for which the present class of chain-doped structures may also serve as a useful experimental platform.

The TLL behavior is characterized by several parameters such as the spin/charge velocities for the collective spin and charge excitations and the anomalous dimension α, which is a function of on-site Coulomb repulsion and v_F. Explicit expressions for these quantities exist in the weak-coupling limit. The Fermi velocity v_F for the noninteracting electrons can be computed by taking the momentum derivative of the band-structure energy: $\hbar v_F = \partial E(k_y)/\partial k_y|_{E_F}$. These are listed in Table II both for the spin-up and -down channels. If we neglect the SOC ($v_{F\uparrow} = v_{F\downarrow} \equiv v_F$) and take the weak coupling limit, then analytical expressions for the characteristic TLL parameters are well-known. With this limit, v_F is also the spin velocity v_s, while the charge velocity is enhanced by the factor $\beta = (1 + V(0)/(\pi\hbar v_F))^{1/2}$. Here, $V(0) = \int_{-\infty}^{\infty} V(x)\, dx$ is the integral of the interaction $V(x)$ in the continuum model and, for a 1D tight-binding model of interacting orbitals, it may be estimated from the expression: $V(0) = a(U + \nu U_1 + \nu U_2 + \dots)$, where $U(U_i)$ is the on-site (near-neighbor) Coulomb repulsion, a is the Mo-Mo distance, and $\nu = 2$ is the number of the various near neighbors. Similarly, the anomalous dimension using the lowest-order perturbation theory [51,52] may be calculated as $\alpha = (V(0)/(2\pi\hbar v_F))^2/2$.

However, in the present case, we are in the strong-coupling limit $U/W \gg 1$, for which there are no analytical expressions for the TLL parameters except in limiting cases. The most studied model in this limit is the one-band Hubbard model in 1D. It was solved exactly by the Bethe ansatz a long time ago for all filling factors n and all values of Coulomb repulsion $U/t \geqslant 0$ [53]. The results show that at half filling, it is always an insulator, while for all other n, we have a metallic system, and the TLL physics is expected to hold. In fact, the $U/t \to \infty$ Hubbard model has been rigorously shown [54] to exhibit the TLL behavior. For other values of U, no rigorous results are available. However, the $t - J$ model, which approximates the Hubbard model in the large U limit with $J = 2t^2/U$, is solvable both at $J/t \to 0$, which is equivalent to the $U \to \infty$ Hubbard model, and at the supersymmetric point $J/t = 2$. In both cases, the model behaves as a TLL [46,55]). Numerical works using exact diagonalization and other techniques have indicated the TLL behavior for a wide range of parameters $0 < J/t \lessapprox 2$ [56,57]. Thus, based on these works, the TLL behavior is expected for the strong-coupling case away from half filling. In fact, several authors have obtained numerical results for the characteristic TLL parameters for the 1D Hubbard model for different values of U/t and band filling n [54]. For $U/W \to \infty$, the anomalous dimension $\alpha = 1/8$ irrespective of the filling factor n [54,58,59]. Since $U/W \sim 5 - 20$ for the compounds studied here, the $U/W \to \infty$ limit is fairly good here.

When SOC is present, its strength of SOC is parameterized by the Fermi velocity difference $(v_{F\uparrow} - v_{F\downarrow})/(v_{F\uparrow} + v_{F\downarrow})$ and the TLL exponent α is modified [47]. The TLL behavior of the 1D Hubbard model with next-nearest-neighbor hopping but without the SOC has been studied using the density-matrix renormalization group [60]. For the chain-doped TMDs, the second-neighbor interaction is substantial and, furthermore, the strength of the SOC can also be tailored by changing the metal dopant M', so these materials can serve as a rich laboratory for studying the TLL behavior.

D. Half-filled defect bands: Mott-Hubbard insulating state and unusual band widening

For the half-filled case, the 1D defect bands would not show the TLL behavior due to the presence of a charge gap for all values of U within the Hubbard model. This is studied below by using the mean-field-based DFT+U formalism. We find two surprising features for the 1D defect bands: (i) Instead of an AFM ground state expected from the Hubbard model physics at half filling, we find that the ground state is usually ferromagnetic. (ii) With U, the bandwidth of the Hubbard bands increases instead of decreasing, which is normally the case for strongly correlated systems where the motion of the electron is inhibited due to correlated motion, resulting in a larger effective mass. The increase of the bandwidth of the Hubbard bands with U can be explained in terms of a multiband model, as discussed below in some detail.

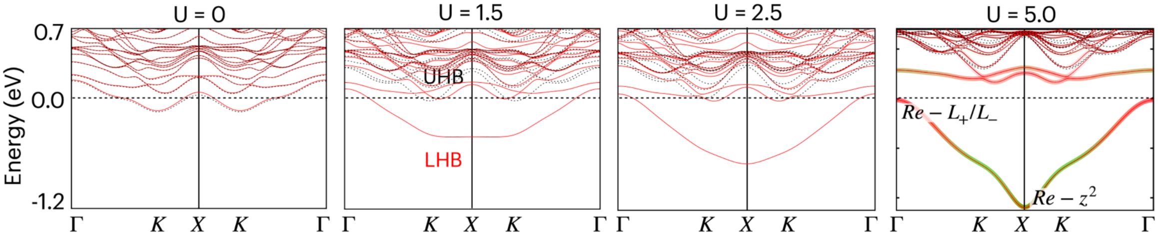

FIG. 8. The DFT+U spin-polarized band structures of MoSe$_2$/Re. The transition to Mott insulating phase occurs through the formation of lower and upper Hubbard bands (LHB and UHB). The LHB widens with U, which is unusual and is interpreted to be due to its multiple-orbital origin.

A plausible explanation for the ferromagnetism is that we don't have an isolated 1D Hubbard chain, rather the electrons are coupled via the electrons of the host materials. In fact, our charge density contour plot in Fig. 3 infers that in the case of MoTe$_2$/Tc there is a covalent bonding between the 1D states with the nearest-neighbor Te-p states of the host material to favor the ferromagnetic ordering.

The band-widening feature can be explained using a multiband Hubbard model. In essence, different parts of the BZ consist of different type of orbitals (for instance, z^2 at K and L^- at Γ for the defect bands as seen from Fig. 1), which can shift around in energy depending on the magnitude of U.

To demonstrate the case of Mott insulating phase and band widening, we examine the case of MoSe$_2$/Re as an example. The nonmagnetic band structure shown in Fig. 7 indicates that the half-filled 1D bands with the bandwidth of about 0.24 eV (see Table II). From spin-polarized DFT + U calculations, we find (see Fig. 8) that with increasing U, the degenerate nonmagnetic half-filled bands spin separate to form a more-occupied lower Hubbard and a less-occupied upper Hubbard band. With further increase in U, the two Hubbard bands separate completely to form a gap, leading to a Mott insulating state. We see similar effects for other chain-doped compounds, which are not shown here to avoid redundancy.

This is in contrast to the conventional Mott insulator, where increasing U makes the Hubbard bands narrower, as the electron's motion becomes restricted due to electron correlation, resulting in a larger effective mass. In the present case, there is a rapid increase in the bandwidth with an increase in U. For example, by increasing U from 0 to 5 eV, the bandwidth has gone from 0.4 eV to 1.1 eV, as can be seen in Fig. 8.

To describe this physics, we have adopted a multiorbital Hubbard model with three orbital basis (z^2, xy, and x^2-y^2), with the Hamiltonian

$$
\begin{aligned}
H = {} & \sum_{i\mu}\epsilon_{i\mu}c^{\dagger}_{i\mu}c_{i\mu} + \sum_{ij;\mu\nu} t_{i\mu j\nu}c^{\dagger}_{i\mu}c_{j\nu} + \text{H.c.} \\
& + U\sum_{i\mu} n_{i\mu\uparrow}n_{i\mu\downarrow} + \left(U' - \frac{J_{\rm H}}{2}\right)\sum_{i\mu<\nu} n_{i\mu}n_{i\nu} \\
& - 2J_{\rm H}\sum_{i,\mu<\nu} S^z_{i\mu}\cdot S^z_{i\nu}. \qquad (4)
\end{aligned}
$$

Here, the first two terms describe the on-site and kinetic energy of the electrons, while the third and fourth terms are the energy cost of having the electrons in the same or different orbitals at the same lattice site. The last term defines the Hund's rule coupling. The relation $U' = U-2J_{\rm H}$ has been used here with J_H/U ratio estimated to be 0.03 based on the agreement between DFT and model band structures. The $n_{i\mu} = n_{i\mu\uparrow} + n_{i\mu\downarrow}$ are the occupation numbers which are obtained from the DFT+U density matrix.

It is too complex to solve the problem for the supercell of MoSe$_2$/Re. Since the defect bands originate from the doped ReSe$_2$ chain and the bulk ReSe$_2$ shows a similar band-widening behavior as well (see Fig. 9), we study the phenomenon for bulk ReSe$_2$ using the multiorbital Hubbard model, Eq. (4).

The results, obtained from both the DFT+U calculations as well as the multiorbital Hubbard model, are shown in Fig. 9. From the top panel in the figure, we observe that for U = 0, it has three spin degenerate bands in the vicinity of the ϵ_F, like in all 2H-TMD compounds. Out of the three, one is completely occupied, another is completely unoccupied, and the third one is a half-occupied band. With an increase in U, the half-occupied band becomes spin nondegenerate. Also, like the case of MoSe$_2$/Re, the lower Hubbard subband becomes more dispersive. The model results, shown in the lower panel of Fig. 9, match very well with the DFT+U results, and the widening of the lower Hubbard band is seen from both

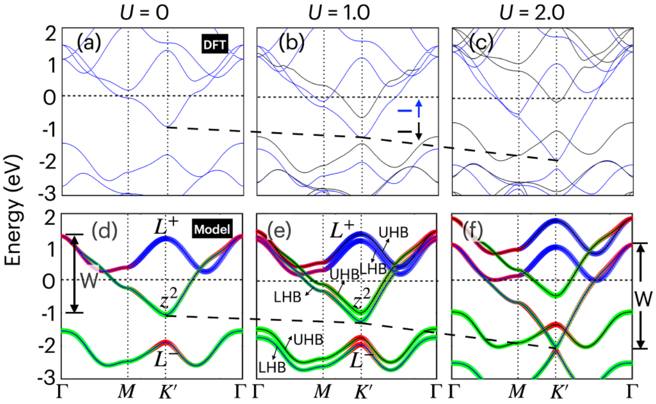

FIG. 9. The spin-polarized band structure of 2H-ReSe$_2$ monolayer as obtained from DFT+U calculations (upper row) and three-orbital-based Hubbard model (lower row) showing excellent agreement. The evolution of the bottom of the LHB with U has been indicated by the dashed line. There is excellent agreement between the model and DFT results. Like the chain-doped system MoSe$_2$/Re (see Fig. 8), the LHB bandwidth, as indicated in (d) and (f), increases with increasing strength of the on-site Coulomb repulsion.

results (indicated by the long-dashed lines). As mentioned already, the lowest conduction band running through E_F has a combination of the orbital characters $L^{\pm}$ (dominant around K') and z^2 (dominated around Γ). The band widening happens because the interorbital interaction term [the fourth term in the Hamiltonian Eq. (4)] lowers the on-site energy for the z^2 orbital (dominant around K'), while increasing the same for the L^+ orbitals (dominant around Γ). In fact, when this term was switched off, there is a band narrowing, clearly seen for the LHB (see Fig. S4 in the SM).

V. SUMMARY

To summarize, by employing DFT calculations and theoretical models, we show that the chain-doped TMDs ($MX_2/M' = M_{n-1}M'_1X_{2n}$), with an M' dopant chain along the zigzag direction, form a sharply localized 1D band structure. While the 1D states are strongly confined along the lateral direction, they are highly mobile along the chain direction. The localization in the lateral direction is interpreted in terms of the bound states of the bare potential of the dopant chain. The partially filled 1D bands provide a platform to explore exotic spin-orbit coupled 1D quantum phases and properties. These include the TLL behavior, ferromagnetic Mott insulator, Rashba-type SOC, and valley-dependent optical transition. The half-filled 1D bands are ideal candidates for stabilizing the antiferromagnetic Mott insulating phase. However, the interaction between the 1D states via the host X-p states makes it ferromagnetic and insulating. When the 1D bands deviate from half filling, the substantial second-neighbor interactions between the M' states make it favorable for practical realization of the TLL behavior. The deviation from half filling can be achieved via impurities and gate biasing.

The widening of the lower Hubbard subband with increasing on-site Coulomb repulsion strength in these chain-doped systems is a nontrivial outcome of this paper. This phenomenon, which is anti-intuitive and goes against the conventional assumption of band narrowing with increasing repulsion strength, has hardly been observed in the literature, which makes this class of materials worth exploring for nontrivial quantum transport and phases. We have explained the cause of band widening by developing a multiorbital Hubbard model. Another important outcome of the present paper is that due to the presence of an intrinsic electric field along the lateral direction, the 1D bands are Rashba spin-split and provide a mechanism to tune the valley-dependent optical transition in MX_2/M'.

Our work opens avenues to tailor 1D quantum physics in 2D TMDs. With the advent of state-of-the-art techniques such as low-energy ion implantation, dislocation climb mechanism, etc., the chain-doped TMDs can be synthesized in a controlled manner. In addition to the electron doping and emergent properties as discussed in this paper, hole doping is also equally likely to introduce interesting features such as orbital and spin Hall effects in such chain-doped compounds. As a whole, we believe that the present paper will excite experimenters and theoreticians alike to envisage exotic quantum phenomena and applications.

ACKNOWLEDGMENTS

This work is funded by the Department of Science and Technology, India, through Grant No. CRG/2020/004330. S.S. thanks SERB India for the VAJRA fellowship. B.R.K.N. acknowledges the support of HPCE, IIT Madras for providing computational facilities.

[1] X. Xi, Z. Wang, W. Zhao, J.-H. Park, K. T. Law, H. Berger, L. Forró, J. Shan, and K. F. Mak, Ising pairing in superconducting NbSe$_2$ atomic layers, Nat. Phys. **12**, 139 (2016).

[2] D. Wickramaratne, S. Khmelevskyi, D. F. Agterberg, and I. I. Mazin, Ising Superconductivity and Magnetism in NbSe$_2$, Phys. Rev. X **10**, 041003 (2020).

[3] E. Revolinsky, G. Spiering, and D. Beerntsen, Superconductivity in the niobium-selenium system, J. Phys. Chem. Solids **26**, 1029 (1965).

[4] P. Li, Y. Wen, X. He, Q. Zhang, C. Xia, Z.-M. Yu, S. A. Yang, Z. Zhu, H. N. Alshareef, and X.-X. Zhang, Evidence for topological type-II Weyl semimetal WTe$_2$, Nat. Commun. **8**, 2150 (2017).

[5] M. N. Ali, J. Xiong, S. Flynn, J. Tao, Q. D. Gibson, L. M. Schoop, T. Liang, N. Haldolaarachchige, M. Hirschberger, N. P. Ong, and R. J. Cava, Large, non-saturating magnetoresistance in WTe$_2$, Nature (London) **514**, 205 (2014).

[6] I. Pletikosić, M. N. Ali, A. V. Fedorov, R. J. Cava, and T. Valla, Electronic Structure Basis for the Extraordinary Magnetoresistance in WTe$_2$, Phys. Rev. Lett. **113**, 216601 (2014).

[7] X. Qian, J. Liu, L. Fu, and J. Li, Quantum spin Hall effect in two-dimensional transition metal dichalcogenides, Science **346**, 1344 (2014).

[8] S. Bhowal and S. Satpathy, Intrinsic orbital and spin Hall effects in monolayer transition metal dichalcogenides, Phys. Rev. B **102**, 035409 (2020).

[9] S. Bhowal and S. Satpathy, Intrinsic orbital moment and prediction of a large orbital Hall effect in two-dimensional transition metal dichalcogenides, Phys. Rev. B **101**, 121112(R) (2020).

[10] L. Zhang, Z. Zhang, F. Wu, D. Wang, R. Gogna, S. Hou, K. Watanabe, T. Taniguchi, K. Kulkarni, T. Kuo, S. R. Forrest, and H. Deng, Twist-angle dependence of moirè excitons in WSe$_2$/MoSe$_2$ heterobilayers, Nat. Commun. **11**, 5888 (2020).

[11] K. Tran, G. Moody, F. Wu, X. Lu, J. Choi, K. Kim, A. Rai, D. A. Sanchez, J. Quan, A. Singh, J. Embley, A. Zepeda, M. Campbell, T. Autry, T. Taniguchi, K. Watanabe, N. Lu, S. K. Banerjee, K. L. Silverman, S. Kim *et al.*, Evidence for moirè excitons in van der Waals heterostructures, Nature (London) **567**, 71 (2019).

[12] P. Wang, G. Yu, Y. H. Kwan, Y. Jia, S. Lei, S. Klemenz, F. A. Cevallos, R. Singha, T. Devakul, K. Watanabe, T. Taniguchi, S. L. Sondhi, R. J. Cava, L. M. Schoop, S. A. Parameswaran, and S. Wu, One-dimensional Luttinger liquids in a two-dimensional moiré lattice, Nature (London) **605**, 57 (2022).

[13] O. Ávalos-Ovando, D. Mastrogiuseppe, and S. E. Ulloa, Lateral interfaces of transition metal dichalcogenides: A stable tunable

one-dimensional physics platform, Phys. Rev. B **99**, 035107 (2019).

[14] H. Zou, X. Wang, K. Zhou, Y. Li, Y. Fu, and L. Zhang, Electronic property modulation in two-dimensional lateral superlattices of monolayer transition metal dichalcogenides, Nanoscale **14**, 10439 (2022).

[15] J. Jia, E. Marcellina, A. Das, M. S. Lodge, B. Wang, D.-Q. Ho, R. Biswas, T. A. Pham, W. Tao, C.-Y. Huang, H. Lin, A. Bansil, S. Mukherjee, and B. Weber, Tuning the many-body interactions in a helical Luttinger liquid, Nat. Commun. **13**, 6046 (2022).

[16] W. Jolie, C. Murray, P. S. Weiß, J. Hall, F. Portner, N. Atodiresei, A. V. Krasheninnikov, C. Busse, H.-P. Komsa, A. Rosch, and T. Michely, Tomonaga-Luttinger Liquid in a Box: Electrons Confined within MoS_2 Mirror-Twin Boundaries, Phys. Rev. X **9**, 011055 (2019).

[17] O. Ávalos-Ovando, D. Mastrogiuseppe, and S. E. Ulloa, Lateral heterostructures and one-dimensional interfaces in 2D transition metal dichalcogenides, J. Phys.: Condens. Matter **31**, 213001 (2019).

[18] D. H. Keum, S. Cho, J. H. Kim, D.-H. Choe, H.-J. Sung, M. Kan, H. Kang, J.-Y. Hwang, S. W. Kim, H. Yang, K. J. Chang, and Y. H. Lee, Bandgap opening in few-layered monoclinic $MoTe_2$, Nat. Phys. **11**, 482 (2015).

[19] G. Kim, S. Song, and D. Jariwala, Spatially controlled two-dimensional quantum heterostructures, Mater. Res. Lett. **11**, 327 (2023).

[20] Y.-C. Lin, R. Torsi, D. B. Geohegan, J. A. Robinson, and K. Xiao, Controllable thin-film approaches for doping and alloying transition metal dichalcogenides monolayers, Adv. Sci. **8**, 2004249 (2021).

[21] E. Kim, C. Ko, K. Kim, Y. Chen, J. Suh, S.-G. Ryu, K. Wu, X. Meng, A. Suslu, S. Tongay, J. Wu, and C. P. Grigoropoulos, Site selective doping of ultrathin metal dichalcogenides by laser-assisted reaction, Adv. Mater. **28**, 341 (2016).

[22] Y.-C. Lin, J. Karthikeyan, Y.-P. Chang, S. Li, S. Kretschmer, H.-P. Komsa, P.-W. Chiu, A. V. Krasheninnikov, and K. Suenaga, Formation of highly doped nanostripes in 2D transition metal dichalcogenides via a dislocation climb mechanism, Adv. Mater. **33**, 2007819 (2021).

[23] M. Barborini, M. Calandra, F. Mauri, L. Wirtz, and P. Cudazzo, Excitonic-insulator instability and Peierls distortion in one-dimensional semimetals, Phys. Rev. B **105**, 075122 (2022).

[24] X.-F. Su, Z.-L. Gu, Z.-Y. Dong, and J.-X. Li, Topological magnons in a one-dimensional itinerant flatband ferromagnet, Phys. Rev. B **97**, 245111 (2018).

[25] P. Hofmann, M. M. Ugeda, A. Tamtögl, A. Ruckhofer, W. E. Ernst, G. Benedek, A. J. Martínez-Galera, A. Stróżecka, J. M. Gómez-Rodríguez, E. Rienks, M. F. Jensen, J. I. Pascual, and J. W. Wells, Strong-coupling charge density wave in a one-dimensional topological metal, Phys. Rev. B **99**, 035438 (2019).

[26] Z. S. Popović and S. Satpathy, Density-functional study of the Luttinger liquid behavior of the lithium molybdenum purple bronze $Li_{0.9}Mo_6O_{17}$, Phys. Rev. B **74**, 045117 (2006).

[27] A. Togo and I. Tanaka, First principles phonon calculations in materials science, Scr. Mater. **108**, 1 (2015).

[28] A. A. Mostofi, J. R. Yates, Y.-S. Lee, I. Souza, D. Vanderbilt, and N. Marzari, Wannier90: A tool for obtaining maximally-localised Wannier functions, Comput. Phys. Commun. **178**, 685 (2008).

[29] See Supplemental Material at http://link.aps.org/supplemental/10.1103/PhysRevB.108.075139 for more information on (a) design of the chain-doped structure, (b) formation energy calculations and (c) model Hamiltonian, and (d) other band structure details.

[30] P. E. Blöchl, Projector augmented-wave method, Phys. Rev. B **50**, 17953 (1994).

[31] G. Kresse and D. Joubert, From ultrasoft pseudopotentials to the projector augmented-wave method, Phys. Rev. B **59**, 1758 (1999).

[32] G. Kresse and J. Furthmüller, Efficient iterative schemes for ab initio total-energy calculations using a plane-wave basis set, Phys. Rev. B **54**, 11169 (1996).

[33] M. Cococcioni and S. de Gironcoli, Linear response approach to the calculation of the effective interaction parameters in the LDA + U method, Phys. Rev. B **71**, 035105 (2005).

[34] P. Giannozzi, S. Baroni, N. Bonini, M. Calandra, R. Car, C. Cavazzoni, D. Ceresoli, G. L. Chiarotti, M. Cococcioni, I. Dabo, A. D. Corso, S. de Gironcoli, S. Fabris, G. Fratesi, R. Gebauer, U. Gerstmann, C. Gougoussis, A. Kokalj, M. Lazzeri, L. Martin-Samos *et al.*, Quantum espresso: A modular and open-source software project for quantum simulations of materials, J. Phys.: Condens. Matter **21**, 395502 (2009).

[35] D. Xiao, G.-B. Liu, W. Feng, X. Xu, and W. Yao, Coupled Spin and Valley Physics in Monolayers of MoS_2 and other Group-VI Dichalcogenides, Phys. Rev. Lett. **108**, 196802 (2012).

[36] S. Manzeli, D. Ovchinnikov, D. Pasquier, O. V. Yazyev, and A. Kis, 2D transition metal dichalcogenides, Nat. Rev. Mater. **2**, 17033 (2017).

[37] T. Chowdhury, E. C. Sadler, and T. J. Kempa, Progress and prospects in transition-metal dichalcogenide research beyond 2D, Chem. Rev. **120**, 12563 (2020).

[38] A. Laturia, M. L. Van de Put, and W. G. Vandenberghe, Dielectric properties of hexagonal boron nitride and transition metal dichalcogenides: from monolayer to bulk, npj 2D Mater. Appl. **2**, 6 (2018).

[39] Z. S. Popovic and S. Satpathy, Wedge-Shaped Potential and Airy-Function Electron Localization in Oxide Superlattices, Phys. Rev. Lett. **94**, 176805 (2005).

[40] S. Tomonaga, Remarks on Bloch's method of sound waves applied to many-fermion problems, Prog. Theor. Phys. **5**, 544 (1950).

[41] K. Schönhammer, Physics in one dimension: Theoretical concepts for quantum many-body systems, J. Phys.: Condens. Matter **25**, 014001 (2012).

[42] J. M. Luttinger, An exactly soluble model of a many-system, J. Math. Phys. **4**, 1154 (1963).

[43] F. D. M. Haldane, 'Luttinger liquid theory' of one-dimensional quantum fluids. I. properties of the Luttinger model and their extension to the general 1D interacting spinless Fermi gas, J. Phys. C **14**, 2585 (1981).

[44] X. G. Wen, Metallic non-Fermi-liquid fixed point in two and higher dimensions, Phys. Rev. B **42**, 6623 (1990).

[45] R. Claessen, M. Sing, U. Schwingenschlögl, P. Blaha, M. Dressel, and C. S. Jacobsen, Spectroscopic Signatures of Spin-Charge Separation in the Quasi-One-Dimensional Organic Conductor TTF-TCNQ, Phys. Rev. Lett. **88**, 096402 (2002).

[46] T. Giamarchi, *Quantum Physics in One Dimension* (Oxford University Press, 2003), Vol. 121.

[47] A. V. Moroz, K. V. Samokhin, and C. H. W. Barnes, Spin-Orbit Coupling in Interacting Quasi-One-Dimensional Electron Systems, Phys. Rev. Lett. **84**, 4164 (2000).

[48] N. Sedlmayr, P. Korell, and J. Sirker, Two-band Luttinger liquid with spin-orbit coupling: Applications to monatomic chains on surfaces, Phys. Rev. B **88**, 195113 (2013).

[49] The TLL behavior of the one-band Hubbard model is suppressed due to the presence of a Mott-Hubbard charge gap exactly at half filling while, for all other fillings, it is a TL liquid.

[50] V. Kozii, J. Ruhman, L. Fu, and L. Radzihovsky, Ferromagnetic transition in a one-dimensional spin-orbit-coupled metal and its mapping to a critical point in smectic liquid crystals, Phys. Rev. B **96**, 094419 (2017).

[51] K. Schonhammer, Interacting fermions in one dimension: The Tomonaga-Luttinger model, arXiv:cond-mat/9710330.

[52] K. Schonhammer, Luttinger liquids: The basic concepts, *Strong Interactions in Low Dimensions* (Springer Netherlands, Dordrecht, 2004).

[53] E. H. Lieb and F. Y. Wu, Absence of Mott Transition in an Exact Solution of the Short-Range, One-Band Model in One Dimension, Phys. Rev. Lett. **21**, 192 (1968).

[54] H. J. Schulz, Correlation Exponents and the Metal-Insulator Transition in the One-Dimensional Hubbard Model, Phys. Rev. Lett. **64**, 2831 (1990).

[55] N. Kawakami and S.-K. Yang, Correlation Functions in the One-Dimensional t-J Mode, Phys. Rev. Lett. **65**, 2309 (1990).

[56] M. Ogata, M. U. Luchini, S. Sorella, and F. F. Assaad, Phase Diagram of the One-Dimensional t-J Model, Phys. Rev. Lett. **66**, 2388 (1991).

[57] A. Moreno, A. Muramatsu, and S. R. Manmana, Ground-state phase diagram of the one-dimensional t-J model, Phys. Rev. B **83**, 205113 (2011).

[58] M. Ogata and H. Shiba, Bethe-ansatz wave function, momentum distribution, and spin correlation in the one-dimensional strongly correlated Hubbard model, Phys. Rev. B **41**, 2326 (1990).

[59] A. Parola and S. Sorella, Asymptotic Spin-Spin Correlations of the $U \to \infty$ One-Dimensional Hubbard Model, Phys. Rev. Lett. **64**, 1831 (1990).

[60] S. Nishimoto, K. Sano, and Y. Ohta, Phase diagram of the one-dimensional Hubbard model with next-nearest-neighbor hopping, Phys. Rev. B **77**, 085119 (2008).